Optimizing transient transport in materials having two scales of porosity

Robert H. Nilson and Stewart K. Griffiths

Physical and Engineering Sciences Center, Sandia National Laboratories, P.O. Box 969, Livermore, California 94550, USA

Porous materials having multiple scales of porosity afford the opportunity to combine the high surface area and functionality of nanopores with the superior charge/discharge characteristics of wider transport channels. However, the relative volume fractions assigned to nanopores and transport channels must be thoughtfully balanced because the introduction of transport channels reduces the volume available for nanopore functionality. In the present paper, the optimal balance between nanopore capacity and system response time is achieved by adjusting the aperture and spacing of a family of transport channels that provide access to adjacent nanopores during recharge/discharge cycles of materials intended for storage of gas or electric charge. A diffusive transport model is used to describe alternative processes of viscous gas flow, Knudsen gas flow, and ion diffusion or electromigration. The coupled transport equations for the nanopores and transport channels are linearized and solved analytically for a periodic variation in external gas pressure, ion concentration, or electric potential using a separation-of-variables approach in the complex domain. Optimization of these solutions yields closed-form expressions for channel apertures and spacing that provide maximum discharge of gas or electric charge for a fixed system volume and a desired discharge time.

PACS number(s): 47.56.+r, 47.61.−k, 89.75.Hc, 82.47.Uv

I. INTRODUCTION

Nanoporous materials are finding increased use in a broad range of emerging technologies including hydrogen and methane storage, gas separation and purification, advanced battery electrodes, electric double layer supercapacitors, desalination membranes, and fuel cell membranes [1–3]. In applications such as these nanoscale pores are beneficial in providing high surface area as well as functionality that, in some cases, can only be obtained at the nanoscale. For example, gases condense to liquids in nanopores at pressures much smaller than the nominal condensation pressure, affording the opportunity for gas storage at high densities but moderate pressure [2]. Similarly, gas separation processes are often based on molecular scale pores that exclude larger species [3] and, in supercapacitor applications, the areal capacitance of subnanometer pores appears to increase with decreasing pore size even though these pores are smaller than the size of a single hydrated ion [4].

Although nanoscale pores provide functionality, they also tend to inhibit the device-scale transport needed to perform rapid charging and discharging of the medium. This is because mass transport velocities of gases and liquids decrease with the square of the pore aperture owing to viscous friction [5]. In addition, a large fraction of an absorbed gas is often nearly immobilized in surface layers reducing the available gas-flow aperture. Similarly, diffusion of ions is inhibited in nanopores [6], particularly in electric double layer capacitors where a large fraction of the ions may reside in relatively immobile surface monolayers [7]. Thus, long range transport in molecular-scale pores is generally detrimental to discharge kinetics.

Multiscale materials that combine nanoscale storage pores with a network of larger scale transport channels afford a promising means for gaining rapid access to a large volume of molecular-scale pores. In these materials, the smallest pores are connected to a family of transport channels having larger apertures and wider spacing. However, since the transport channels lack the desired nanopore surface area and functionality there will be a corresponding loss of nanopore volume available for gas storage capacity, electric capacitance, or catalytic surface area. To resolve this conflict, the present paper seeks to identify channel configurations that provide an optimal balance between system capacity and rapid access time.

Previous studies aimed at optimizing transport in multi-scale networks have addressed steady flow processes in branching networks such as those occurring naturally in vascular networks [8], leaf veins [9], and river drainage basins [10]. The same physics are operative in branching networks that supply water, gas, and electricity to industrial societies [11] and in engineered materials that are intended to provide optimal heat extraction [12], fluid distribution [13], or catalysis [14]. Systems such as these are typically constructed in a manner that minimizes the work required to supply a system of given size subject to constraints on the volume of circulating fluid or the cost of materials needed to construct the network. Previous studies of this optimization problem have identified relationships between channel sizes and lengths in different levels of the hierarchical branching structure and how these features scale with the overall system size [8,10,15–17]. Similarly, the channel structures of porous catalytic beds have been optimized to obtain the maximum reaction rate for a given reactant flow rate [14]. In addition, some prior studies have sought to explain network structures observed in nature by analysis of evolutionary processes such as mechanical instabilities [9] or erosion processes [10] that produced the network. These two competing theories of optimization and evolution are juxtaposed in the "constructal theory" of Bejan and Lorente [13,18] which postulates that configurations must evolve in a way that provides easier access to the currents that flow through it.

Unlike those previous studies of steady-state transport, the present paper addresses transient processes where the goal is to achieve maximal extraction of gas or electrical charge
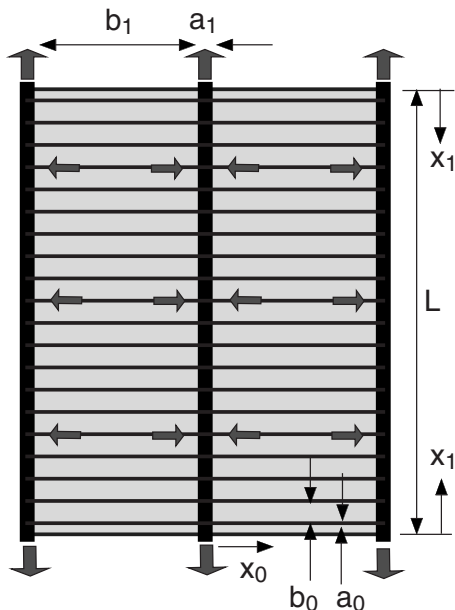
FIG. 1. Geometry of latticelike network having two scales of porosity.

from a nanoporous energy storage material of given size in a prescribed time period. Networks optimized for transient processes like this differ from their steady counterparts because the transient response times of diffusionlike processes increase with the square of channel length while steady pressure drops increase linearly with channel length.

Another distinguishing feature of the present work is a latticelike network topology intended to facilitate transport from the interior of a storage reservoir to its boundaries, as illustrated in Fig. 1. This network architecture differs fundamentally from branching networks that connect a centrally located point source to its surroundings. By design, the present lattice network has connectivity similar to that in packed beds where a gas flows through large channels between particles and then into the smaller pores within the particles. The same sort of connectivity can now be engineered into nanoporous materials using advanced fabrication processes that produce multiple scales of porosity by phase segregation, templating, and multiscale aggregation processes [19].

In an effort to explore fundamental principles in a very simple context, we address diffusionlike processes in a two-dimensional network of slitlike channels. This permits the use of analytical solutions to describe the transient multiscale transport induced by a sinusoidal variation in the external pressure or electric potential. These analytical results serve as the basis for derivation of closed-form expressions for the optimal aperture and spacing of transport channels.

II. GOVERNING EQUATIONS

Consider a highly idealized nanoporous material comprised of permeable slabs separated by an array of parallel planar channels having uniform aperture a_1 and center-to-center spacing b_1, as illustrated schematically in Fig. 1. The

slitlike nanopores within the slabs have a characteristic aperture and spacing of a_0 and b_0, and hence a bulk porosity of $\phi_0 = a_0/b_0$. Gas flow or ion transport within each of the nanopores can generally be described by an equation of the form [5,20–23]

$$\beta_0 \frac{\partial \rho}{\partial t} = \frac{\partial}{\partial x_0}\left(D_0 \frac{\partial \rho}{\partial x_0}\right), \tag{1}$$

where x_0 is the distance from the pore entrance, t is the time, ρ is the density of gas molecules or ions, and D_0 is the effective diffusion coefficient for transport within an individual pore. The capacitance β_0 is typically unity in gas transport applications but may take other values to account for surface adsorption or capacitance in small pores, as explained below. Distinct from the diffusion coefficient, D_0, the effective diffusivity is defined as $\alpha_0 = D_0/\beta_0$.

In a gas flow, the apparent rate of diffusion is limited by collisions among gas molecules and by collisions with pore walls. When the mean free path Λ is small compared to the pore aperture a_0, collisions among gas molecules predominate and $D_0 = a_0^2 P/12\mu$ where P is the pressure and μ is the viscosity [5,20,21]. This diffusivity can also be written as $D_0 = \kappa P/\mu\phi_0$ in terms of a known value of the bulk permeability κ of the matrix slabs. Another flow regime applies when the mean free path is large compared to the pore aperture. In this instance the appropriate diffusion coefficient is given by the Knudsen expression, $D_0 \propto \nu a_0$, in which $\nu = (8kT/\pi m)^{1/2}$ is the mean thermal speed. The constant of proportionality in this expression for D_0 is simply 1/3 for a circular channel but varies as $\ln(\Lambda/a_0)/\sqrt{8}$ for slitlike pores [5,20,21]. Furthermore, in very small pores measuring only one or two molecular diameters, an even slower regime of free molecular diffusion has been identified by Jepps *et al.* [22].

Ion transport within the porous electrodes of electrochemical capacitors can also be described by Eq. (1). Here, the operative processes of diffusion and electromigration are respectively driven by axial gradients of ion concentration and electric potential along electrolyte-filled pores [23,24]. However, since the local electric potential is related to the surface charge density [25], either mechanism can be modeled as a diffusionlike process in which the effective diffusion coefficient, D_0, is either the ion diffusion coefficient or ion mobility. Here, much of the electric charge is stored in one or two molecular layers adjacent to the pore walls. Thus, the effective capacitance in Eq. (1) is roughly proportional to the wetted perimeter divided by the cross sectional area, i.e., $\beta_0 \propto 2/a_0$ [24,25]. As a result, the diffusivity, $\alpha_0 = D_0/\beta_0$, tends to increase linearly with pore size. In addition, the effective diffusivity in small pores may increase with increasing pore size due to mitigation of hindrance effects that occur when pore sizes are comparable to the sizes of hydrated ions [6]. The central point is that the effective diffusivities of ions or gas molecules may often increase with channel size, thus motivating the introduction of transport channels into nanoporous storage materials.

Transport along the vertical transport channels in Fig. 1 is governed by an equation that resembles Eq. (1) but also in-

cludes lateral transport between these channels and the adjacent nanopores,

$$\beta_1 \frac{\partial \rho}{\partial t} = \frac{\partial}{\partial x_1}\left(D_1 \frac{\partial \rho}{\partial x_1}\right) + \frac{2\phi_0}{a_1}D_o \left.\frac{\partial \rho}{\partial x_0}\right|_{x_0=0}. \qquad (2)$$

Here, x_1 is measured from the channel entrances at system boundaries and the factor of $2/a_1$ in the last term represents the ratio of surface area to cross-sectional area for a slitlike channel. In addition, the lateral diffusion flux in the last term is multiplied by ϕ_0 as this represents the fraction of channel wall area receiving lateral transport. The effective gas diffusion coefficient is given by $D_1 = Pa_1^2/12\mu$ or by $D_1 \sim \nu a_1$ for the viscous and Knudsen regimes, respectively, as explained above. Thus, wider channels have larger diffusion coefficients whenever $\alpha_1 > \alpha_0$ and the same holds true for ion transport. To facilitate analytical solution we will assume that the diffusion coefficients D_k and diffusivities $\alpha_k = D_k/\beta_k$ are each constant within pores of the same family.

To model the discharge/recharge cycle of energy storage materials we seek solutions of the following form appropriate for a sinusoidal variation in the external density having a frequency ω, amplitude $\Delta\rho$, and mean value ρ_r,

$$\rho^* = \frac{\rho - \rho_r}{\Delta\rho} = \text{Re}[e^{i\omega t}\rho_0^*(x_0^*)\rho_1^*(x_1^*)]. \qquad (3)$$

Here, $\rho_0^*(x_0^*)$ represents the variation of ρ^* along the nanopores, $\rho_1^*(x_1^*)$ is the variation along transport channels, $x_0^* = 2x_0/b_1$, $x_1^* = 2x_1/L$, $i \equiv \sqrt{-1}$, and Re indicates the real part of a complex number. This approach, referred to as complex combination [26], is a separation-of-variables technique in which the spatially varying functions, $\rho_0^*(x_0^*)$ and $\rho_1^*(x_1^*)$, are complex in character and can thus represent both the amplitude and the phase relation of the response to a periodic forcing function. We chose to investigate a periodic response, rather than a step response, largely for analytical simplicity with the expectation that optimized pore structures would be relatively insensitive to this distinction. In either case, the optimal structures are expected to be quite sensitive to the desired discharge period, here π/ω.

Substitution of Eq. (3) into Eq. (1) yields a second-order ordinary differential equation for $\rho_0^*(x_0^*)$,

$$ib_1^{*2}\rho_0^* = \frac{d^2\rho_0^*}{dx_0^{*2}} \qquad (4)$$

subject to the boundary condition $\rho_0^* = 1$ at the interface between channels and slabs where $x_0^* = 0$ and the symmetry condition $(\rho_0^*)' = 0$ at the slab midplane where $x_0^* = 1$. The solution is

$$\rho_0^*(x_0^*) = \frac{\cosh b_1^*\sqrt{i}(1 - x_0^*)}{\cosh b_1^*\sqrt{i}} \quad \text{where} \quad b_1^* \equiv \frac{b_1}{2}\sqrt{\frac{\omega}{\alpha_0}}. \qquad (5)$$

The normalized transport channel spacing b_1^* may be viewed as a Fourier modulus representing the ratio of the nanopore half-length, $b_1/2$, to the diffusion distance $\sqrt{\alpha_0/\omega}$ traversed in a time of $1/\omega$. Equivalently, it is the square root of the diffusion time $(b_1/2)^2/\alpha_0$ divided by the cycle time. Simi-

larly, substitution of Eqs. (3) and (5) into Eq. (2) yields the following result for the transport channels:

$$\rho_1^*(x_1^*) = \frac{\cosh \hat{L}^*\sqrt{i}(1 - x_1^*)}{\cosh \hat{L}^*\sqrt{i}}. \qquad (6)$$

The form of this expression is identical to the preceding equation for $\rho_0^*(x_0^*)$ except that the applicable Fourier modulus, $\hat{L}^*$, is now given by

$$\hat{L}^* = L^*\left[\frac{\alpha_0}{\alpha_1}\left(1 + \frac{\hat{\phi}_o b_1^*}{a_1^*}\frac{\tanh b_1^*\sqrt{i}}{b_1^*\sqrt{i}}\right)\right]^{1/2}, \qquad (7)$$

where

$$L^* \equiv \frac{L}{2}\sqrt{\frac{\omega}{\alpha_0}} \quad \text{and} \quad \hat{\phi}_0 \equiv \phi_0\frac{\beta_0}{\beta_1}. \qquad (8)$$

In the above equations, a_1^*, b_1^*, and L^* have all been normalized by the length scale $\sqrt{4\alpha_0/\omega}$. Also, by inspection of Eq. (7) we see that for small b_1^*, $\tanh b_1^*\sqrt{i}/b_1^*\sqrt{i} \rightarrow 1$ and the apparent diffusivity along transport channels is reduced by a factor of $(a_1^* + b_1^*\hat{\phi}_0)/a_1^*$ representing the ratio of the total capacitance to that within the transport channels. This is the expected behavior when all of the nanopore volume always remains nearly in local equilibrium with the transport channels.

The diffusivity ratio, α_0/α_1, appearing in Eq. (7) can either be prescribed as a known constant or it can be expressed as follows in terms of the normalized pore apertures:

$$\left(\frac{\alpha_0}{\alpha_1}\right) = \left(\frac{a_0}{a_1}\right)^m = \left(\frac{a_0^*}{a_1^*}\right)^m. \qquad (9)$$

As explained earlier, $m = 2$ for a viscous gas flow, $m \sim 1$ for free molecular gas flow, and $m = 0$ for a simple diffusion process. We also noted earlier that these exponents increase by unity when the capacitance is associated mainly with the channel surface area, rather than the channel volume. This is often the case in nanoporous gas storage materials where surface adsorption provides the primary capacitance [2,22] and in electrochemical capacitors where electric charge is accumulated in surface layers having a thickness of one or two molecular diameters [7,24]. Thus, our example calculations will explore the range $0 \leq m \leq 3$.

The pore structure is optimized by adjusting the values of a_1^* and b_1^* to obtain the maximum cyclical inflow/outflow from the nanopores subject to a given system volume. Maximizing cyclical flow is equivalent to maximizing the amplitude of the sinusoidal variation in the mean density within the nanopores, $|\Delta\bar{\rho}_0^*|$. This quantity is readily evaluated by spatial integration of the solution given by Eqs. (3) and (5)–(8) over the nanopore volume to obtain

$$|\Delta\bar{\rho}_0^*| = \text{mod}\left[\frac{\tanh b_1^*\sqrt{i}}{b_1^*\sqrt{i}}\frac{\tanh \hat{L}^*\sqrt{i}}{\hat{L}^*\sqrt{i}}\right]. \qquad (10)$$

Here, the modulus is the amplitude the complex number in brackets and so represents half of the peak to valley variation of the mean nanopore density. Because the nanopores gener-

ally provide functionality or capacitance unavailable in wider transport channels, we take credit only for density changes within the nanoporous matrix blocks. Thus, the optimization criterion, Ω^*, is taken as the product of $|\Delta\bar{\rho}_0^*|$ with the ratio of the volume containing nanopores, Lb_1, to the total system volume, $L(a_1+b_1)$,

$$\Omega^* = |\Delta\bar{\rho}_0^*|\frac{V_{\text{nanopores}}}{V_{\text{total}}} = |\Delta\bar{\rho}_0^*|\frac{1}{1+a_1^*/b_1^*}. \tag{11}$$

The nanopore porosity, ϕ_0, and capacitance, β_0, need not be included in the numerator of this objective function because they are constants for nanopores of fixed size and so do not influence the optimization. By omitting these constants, we ensure that the object function, Ω^*, will have a maximum value of unity when two conditions are met: the potential within the nanopores closely tracks the applied external potential ($|\Delta\bar{\rho}_0^*| \to 1$), and the volume lost to transport channels is negligible ($a_1^*/b_1^* \to 0$). Note that increases in a_1^* or decreases in b_1^* help to increase the term $|\Delta\bar{\rho}_0^*|$ in the numerator of Eq. (11) but these variations also tend to increase the denominator. As a result, Ω^* has a maximum value for optimal choices of a_1^* and b_1^*.

III. RESULTS

A particular configuration to be optimized is specified by prescribing values of the normalized nanopore aperture, a_0^*, and the normalized system scale, L^*. In addition to these parameters, one must also specify the value of the quantity $\hat{\phi}_0 \equiv \phi_0\beta_0/\beta_1$ appearing in Eq. (7). This parameter will be treated as a constant, since the nanopore porosity, ϕ_0, and the capacitance values, β_0 and β_1, are often known constants. In gas flows, both β's are typically unity. Further, in cases where surface capacitance is important, this mechanism will often be dominant only in the nanopores where surface storage layers measuring only one or two molecular diameters represent a substantial fraction of the pore aperture, a_0. In this instance, β_0 is computed for the prescribed value of a_0 and the value of β_1 (often unity) is typically independent of the yet to be optimized, a_1.

Finally, the variation in diffusivity with channel aperture is given by the parameter, m, appearing in the power-law relation of Eq. (9). We will first address cases where the diffusivity varies with channel aperture ($m=1,2,3$). Later, we consider the degenerate case ($m=0$) where the diffusivity of the transport channels is independent of their apertures. In this circumstance we prescribe a fixed ratio of diffusivity between transport channels and nanopores.

A. Power-law variation in diffusivity with channel aperture ($m > 0$)

As seen in Fig. 2, the normalized values of the optimal channel apertures and spacing both increase with the normalized system size, L^*. The nearly constant slopes on the logarithmic plot of Fig. 2 indicate power-law variations of the form
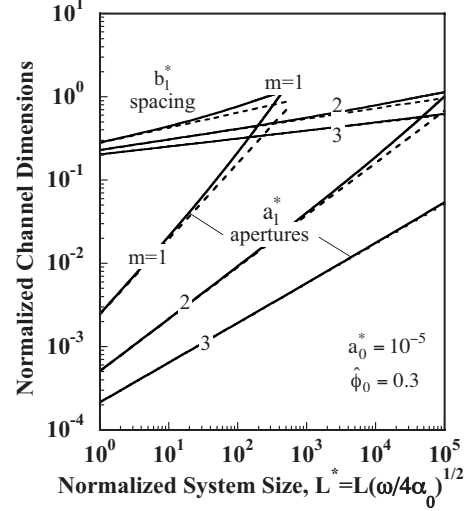

FIG. 2. Variation in optimized channel apertures (lower three lines) and channel spacing (upper three lines) with system scale. Solid lines are numerical optimization. Dotted lines are series expansion.

$$a_1^* = AL^{*p} \quad \text{and} \quad b_1^* = BL^{*q}. \tag{12}$$

It is surprising to see in Fig. 2 that these asymptotes apply over several decades, extending nearly to the point where optimal apertures approach optimal spacing; at this intersection half of the system volume is devoted to transport channels. The exponents appearing in Eq. (12) have the following values: $(p,q) = (10/11,\ 2/11),\ (5/8,\ 1/8)$, and $(10/21,\ 2/21)$ for $m=1,2$, and 3, respectively. Note that in all cases $p=5q$, indicating variations in aperture much greater than those in spacing. The exponents quoted above were originally estimated from the slopes of numerically calculated results in Fig. 2, but they were then verified and refined by the analysis described below.

Analytical expressions for the powers and constants appearing in Eq. (12) were determined by substitution of the assumed power-law forms of Eq. (12) into the objective function, Ω^*. To optimize, derivatives of this expression with respect to the constants, A and B, were then equated to zero. Both of the resulting nonlinear equations were then expanded as a power series in L^*, yielding the following pair of equations for the lowest order terms:

$$5AB^4(m+1)\hat{\phi}_0(a_0^*A)^mL^{*p(m+1)+4q+2} - 45A^{2m+3}L^{*p(2m+3)}$$
$$+ 7B^3(m+1)a_0^{*2m}\hat{\phi}_0^2L^{*3q+4} = 0, \tag{13}$$

$$15A^{m+1}B^4\hat{\phi}_0a_0^{*m}L^{*p(m+1)+4q+2} - 45A^{2m+3}L^{*p(2m+3)}$$
$$+ 7B^3a_0^{*2m}\hat{\phi}_0^2L^{*3q+4} + 14A^{2(m+1)}B^5L^{*2p(m+1)+5q} = 0. \tag{14}$$

To satisfy either of these equations requires a balancing of the single negative term in each against at least one positive term of the same order in L^*. Thus, the exponent of L^* in the second term of Eq. (13) must match that of the first or third terms, requiring that $p(m+1)+4q+2=p(2m+3)$ and/or

$p(2m+3)=3q+4$. Applying the same reasoning to the second equation yields three more candidate equations for p and q. However, it can be readily seen that three of the exponents appearing in Eq. (13) are repeated in Eq. (14), leaving a maximum of three independent equations for the unknown powers, p and q. In general we would need to select the pair of candidate equations that strikes a balance between the leading order terms and leaves one or more higher-order term that can then be neglected. Remarkably, for the present problem, only two of the candidate relations between p and q are linearly independent. Thus, satisfaction of any linearly independent pair ensures equality of all exponents in both equations. For example, the pair of equations in the text just below Eq. (14) yields the following values for the powers, p and q:

$$p = \frac{10}{6+5m} \quad \text{and} \quad q = \frac{p}{5} = \frac{2}{6+5m}. \quad (15)$$

For these choices, all of the terms in Eqs. (13) and (14) are of the same order in L^*.

Having determined the appropriate values of the powers, p and q, the common multiplier involving L^* can be divided out of Eqs. (13) and (14), leaving a pair of equations for the unknown constants, A and B, in terms of the parameters a_0^*, $\hat{\phi}_0$, and m. The positive real roots of these equations are incorporated into the expressions given below in Eqs. (16) and (17) for $m=1$, Eqs. (18) and (19) for $m=2$, and Eqs. (20) and (21) for $m=3$,

$$a_1^* = \left[\frac{(37\sqrt{417}-675)a_0^{*5}\hat{\phi}_0^5 L^{*10}}{26\,254\,935(26\,695-1321\sqrt{417})} \right]^{1/11}$$

$$\approx 0.78767[a_0^*\hat{\phi}_0 L^{*2}]^{5/11}, \quad (16)$$

$$b_1^* = \left[\frac{675(1321\sqrt{417}-26\,695)a_0^*\hat{\phi}_0 L^{*2}}{702\,464} \right]^{1/11}$$

$$\approx 0.88766[a_0^*\hat{\phi}_0 L^{*2}]^{1/11}, \quad (17)$$

$$a_1^* = \left[\frac{4a_0^{*10}\hat{\phi}_0^5 L^{*10}}{5} \right]^{1/16} \approx 0.98615[a_0^{*2}\hat{\phi}_0 L^{*2}]^{5/16}, \quad (18)$$

$$b_1^* = \left[\frac{125a_0^{*2}\hat{\phi}_0 L^{*2}}{64} \right]^{1/16} \approx 1.04273[a_0^{*2}\hat{\phi}_0 L^{*2}]^{1/16}, \quad (19)$$

$$a_1^* = \left[\frac{(486\,305+15\,529\sqrt{1201})a_0^{*15}\hat{\phi}_0^5 L^{*10}}{288\,120} \right]^{1/21}$$

$$\approx 1.06227[a_0^{*3}\hat{\phi}_0 L^{*2}]^{5/21}, \quad (20)$$

$$b_1^* = \left[\frac{50\,625(10\,540\,927+281\,975\sqrt{1201})^{21}a_0^{*3}\hat{\phi}_0 L^{*2}}{8\,605\,184(486\,305+15\,529\sqrt{1201})^{25}} \right]^{1/21}$$

$$\approx 1.11226[a_0^{*3}\hat{\phi}_0 L^{*2}]^{1/21}. \quad (21)$$

The validity and applicable range of the above one-term expansions is illustrated in Fig. 2 where analytical results (dotted lines) are found to be in excellent agreement with numerically optimized values of aperture and spacing (solid lines). Indeed, for $m=3$, the two sets of results are indistinguishable over the full range shown. Also, inspection of the preceding Eqs. (16)–(21) reveals that they can all be written in the following form:

$$a_1^* \approx [a_0^{*m}\hat{\phi}_0 L^{*2}]^{5/(6+5m)} \quad \text{and} \quad b_1^* \approx [a_0^{*m}\hat{\phi}_0 L^{*2}]^{1/(6+5m)}. \quad (22)$$

Here, the only approximation we make is to replace the leading constants with unity. In doing so, we incur average and maximum errors of about 10% and 20%, respectively.

The normalized optimal spacing between transport channels, b_1^*, is seen to increase very slowly with L^* since the corresponding power, $q=1/(6+m)$ is generally quite small. The physical basis for this can be understood by recalling that b_1 is not only the spacing between transport channels; it is also the length of the nanopores having fixed apertures a_0 and fixed diffusivity α_0 (see Fig. 1). Accordingly, the Fourier modulus b_1^* represents the nanopore half-length $b_1/2$ divided by the depth of diffusion, $\sqrt{\alpha_0/\omega}$, into the nanopores during the extraction time, $\sim 1/\omega$. Thus, if b_1^* becomes too large, remote portions of the nanopores will become unresponsive to an external disturbance. Now, the fractional degree of the volumetric flow response within the nanopores is expressed by the ratio, $\tanh b_1^*\sqrt{i}/b_1^*\sqrt{i}$, appearing in Eqs. (7) and (10). Also, this ratio ranges from about 0.99 to 0.76 as b_1^* increases from about 0.2 to 1.0 in Fig. 2. Thus, smaller values of b_1^* could only provide a slight improvement of 1% in volumetric flow, while much larger values would degrade the volumetric flow by a factor of roughly $1/b_1^*$, since $\tanh b_1^*/b_1^* \approx 1/b_1^*$ for $b_1^* > 2$. As a result, optimal values of b_1^* generally span less than an order of magnitude from about 0.2 to 2.0.

In contrast, the optimal aperture of transport channels, a_1^*, spans several orders of magnitude for the range of L^* shown in Fig. 2. The physical basis for this is the need to maintain moderate ($\sim 0.2-2.0$) values of the other Fourier modulus, $\hat{L}^*$, that controls equilibration along the transport channels. This situation is analogous to that of the preceding paragraph except that the length scale, L, appearing in the Fourier modulus $\hat{L}^*$ is now prescribed; it cannot be adjusted. But here we have the freedom to adjust the transport channel aperture, a_1^*, and hence the diffusivity, α_1, appearing in $\hat{L}^*$. The required variation in a_1^* can be roughly estimated from the definition of the Fourier modulus, $\hat{L}^*$, in Eq. (7). To maintain an order-unity value of $\hat{L}^*$ requires that

$$a_1^* \propto L^{*2/(1+m)} \propto L^{*10/(5+5m)}. \quad (23)$$

This is obtained by assuming that b_1^* is essentially constant and that $\tanh b_1^*/b_1^* \approx 1$, consistent with the preceding paragraph. This estimate of $p \approx 10/(5+5m)$ for the power-law exponent of a_1^* is remarkably close to the exact value of $p=10/(6+5m)$ given earlier in Eq. (13). Note that the exponent in Eq. (23) varies from about 1.0 to 0.5 for $m=1$ to 3, requiring that a_1^* vary by several orders of magnitude when
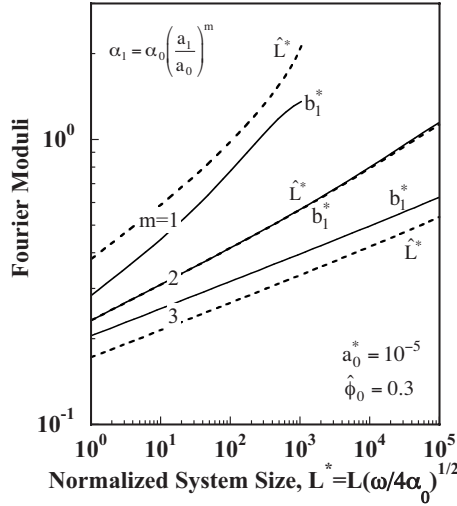
FIG. 3. Fourier moduli indicate ratio of transport time to discharge cycle time for nanochannels, b_1^*, and transport channels, $\hat{L}^*$. Optimized moduli for the two scales are comparable but not always identical.

L^* ranges over the 5 orders of magnitude shown in Fig. 2. Thus, the weak variation in b_1^* and the much stronger variation in a_1^* with L^* can both be explained by the need to maintain values of the Fourier moduli ranging from about 0.2 to 2.

The two Fourier moduli, b_1^* and $\hat{L}^*$, are both displayed in Fig. 3 as a function of L^*. As noted in the preceding paragraph, the quantities $(\tanh b_1^* \sqrt{i})/b_1^* \sqrt{i}$ and $(\tanh \hat{L}^* \sqrt{i})/\hat{L}^* \sqrt{i}$ represent the fractional flow response or, equivalently, the density amplitude ratios (mean variation/entrance amplitude) within the nanopores and along the transport channels, respectively. Thus, the observed equality of the optimal b_1^* and $\hat{L}^*$ for $m=2$ indicates that the two scales of transport have equal variations in potential (pressure or electric potential) and hence equal transport resistance or, equivalently, equality of transient response time. For values of m other than 2, the two Fourier moduli are comparable but not exactly equal. In the limit of small L^*, the ratio of the moduli converges to

$$\frac{\hat{L}^*}{b_1^*} = \left(\frac{2}{m}\right)^{1/2}. \tag{24}$$

Moreover, these ratios of optimal moduli remain relatively constant over the full range of L^* as illustrated by the parallelism of the pairs of lines in Fig. 3.

Physically, optimal performance requires that both scales of the network, nanopores and transport channels, must have comparable response times, or equivalently, comparable values of Fourier modulus. If the nanoscale responds much slower than the system scale, performance can generally be improved by reducing the length of the nanopores, b_1, while also reducing the aperture, a_1, of the transport channels. These changes drive the two Fourier moduli, or normalized time constants, toward one another while also maintaining a relatively constant value of the porosity, $\phi_1 = a_1/b_1$, allocated to the transport channels. However, the optimal Fourier
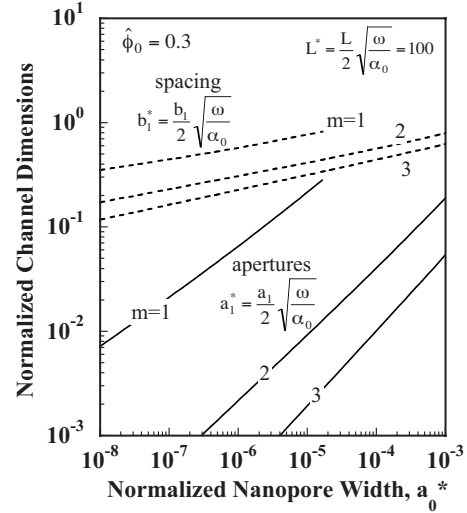

FIG. 4. Variation of optimized channel apertures (solid lines) and channel spacing (dotted lines) with normalized nanopore width, a_0^*.

moduli need not be identical because the relative benefits of adjustments in a_1^* and b_1^* depend upon the exponent m that describes the sensitivity of diffusivity α_1 to changes in aperture, a_1^*. When $m > 2$, increases in a_1^* provide greater relative benefits which tends to favor larger apertures, leading to, $\hat{L}^* < b_1^*$ consistent with Fig. 3. Conversely, values of $m < 2$ lead to optimal solutions with $\hat{L}^* > b_1^*$. In the special case of $m=2$, both Fourier moduli have a linear sensitivity to their respective geometric parameters since $b_1^* \propto b$ and $\hat{L}^* \propto 1/a^{m/2}$ under the constraint of a fixed value of the porosity, $\phi_1 = a_1^*/b_1^*$.

The variation in optimal channel dimensions with the normalized nanopore aperture a_0^* is shown in Fig. 4 for $L^* = 100$. As in the earlier Fig. 2, power-law dependence spans the entire parameter range. Optimal aperture and spacing are both found to increase with increasing a_0^*. Since the diffusivities of transport channel are proportional to $(a_1^*/a_0^*)^m$, it follows that their apertures would have to increase with increasing a_0^* in order to provide the diffusivity needed to maintain an order-one value of the Fourier modulus $\hat{L}^*$. This expectation of roughly constant $\hat{L}^*$ together with the approximations that led to the earlier Eq. (23) can be used to make the estimate that $a_1^* \propto a_0^{*m/(1+m)}$ which is very close to the exact relationship $a_1^* \propto a_0^{*5m/(6+5m)}$ in Eq. (22). A similar argument would suggest that b_1^* should be relatively independent of a_0^*, consistent with Fig. 4 and with the exponent of $m/(6+5m)$ in Eq. (22). However, this constancy of b_1^* tends to obscure the fact that the physical value of the optimal channel spacing, b_1, does depend rather strongly upon the physical value of the nanopore aperture, a_0. This dependence is implicit in our results because the scaling of b_1^* involves the diffusivity α_0 which, in turn, depends upon a_0. This scaling is chosen to emphasize the role of the associated Fourier moduli and to permit application to any process where $\alpha_0 \propto a_0^m$.

The dependence of optimal apertures and spacing on physical, rather than normalized, variables is revealed by rewriting Eq. (22) in the physical form

$$a_1 = L^p (a_0^m \hat{\phi}_0)^{p/2} \left(\frac{\omega}{4\alpha_0} \right)^{p/5}$$

and

$$b_1 = L^{p/5} (a_0^m \hat{\phi}_0)^{p/10} \left(\frac{4\alpha_0}{\omega} \right)^{p(1+m)/5}. \tag{25}$$

By now introducing the relationships $\alpha_0 = \psi_0 a_0^m$ and $p = 10/(6+5m)$ we arrive at the following expressions for the optimal aperture and spacing in terms of primitive variables:

$$a_1 = (L^2 \hat{\phi}_0)^{5/(6+5m)} a_0^{3m/(6+5m)} \left(\frac{\omega}{4\psi_0} \right)^{2/(6+5m)}$$

and

$$b_1 = (L^2 \hat{\phi}_0)^{1/(6+5m)} a_0^{m(3+2m)/(6+5m)} \left(\frac{4\psi_0}{\omega} \right)^{2(1+m)/(6+5m)}. \tag{26}$$

Here, ψ_0 is a constant that can be readily computed for any of the applications described earlier. It is seen in Eq. (26) that the exponent for the variation in b_1 with a_0 [i.e., $m(3+2m)/(6+5m)$] is very close to $m/2$, the value needed to maintain a constant value of the Fourier modulus, $b_1^* \propto b_1/\alpha_0^{1/2} \propto b_1/a_0^{m/2}$. Similarly, to maintain a constant value of the modulus $\hat{L}^*$ defined in Eq. (7) requires a variation of the form $a_1 \approx a_0^{m/2(m+1)}$. This exponent is again very close to the exact value of $3m/(6+5m)$ given in Eq. (26).

The cycle frequency, ω, or equivalently the discharge period, $\tau = \pi/\omega$, also has a strong influence on optimal channel dimensions. With increasing frequency, the channel spacing, b_1, must get smaller so that the nanopores will be short enough to permit equilibration in a shorter time. According to Eq. (26), this dependence is roughly $b \propto 1/\omega^{2/5}$, slightly weaker than the square root dependence needed to maintain a constant b_1^*. This reduction in spacing with increasing ω helps to reduce the flow carried by each of the transport channels, reducing the need for large transport channel apertures. Despite this, a moderate increase in channel aperture, a_1, is still needed to maintain optimal conditions at higher frequencies.

Because optimal parameters depend upon the cycle frequency, there can be no storage material that is optimal for all time scales. If lengthy recharge and discharge times are acceptable (small ω), the optimum material will generally have relatively narrow and widely spaced transport channels, leaving more of the system volume available for nanopore storage. Conversely, a rapid response (large ω) will require closely spaced transport channels with wider apertures, leaving less volume for nanopore storage. This sensitivity to time scales is not a consequence of our methodology, but rather a consequence of the controlling physical processes. Fortunately, the desired time scale is often known. If not, the channel dimensions can be optimized for the central part of a desired range, makings sure that performance is still acceptable at the extremes of the operating window.

Figure 5 depicts the variation in the optimal value of the transport efficiency, Ω^*, with normalized system scale, L^*. Recall that a value of $\Omega^* = 1$ indicates that the density within nanopores precisely tracks the imposed external density
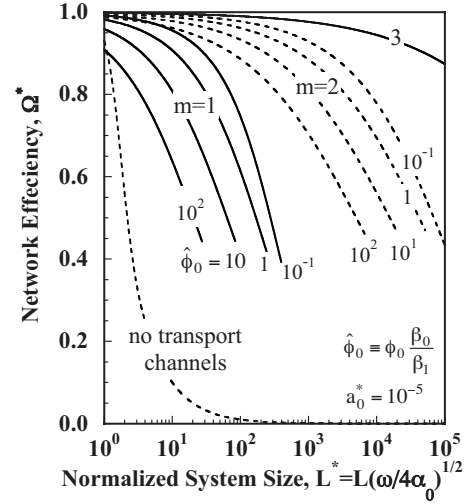

FIG. 5. Network efficiency, Ω^*, indicates optimal discharge from a storage medium for given normalized system scale, L^*, relative to maximum possible under ideal conditions where $L^* \rightarrow 0$.

variation and that the volume lost to the transport channels is negligible. This is the best possible performance. The dotted line in the bottom left corner of Fig. 5 shows that, in the absence of transport channels, the transport efficiency falls below $\Omega^* = 0.5$ for domain sizes greater than $L^* = 2$, indicating that less than 50% of the maximum possible extraction is achieved. In contrast, for the case of $m = 3$ and $\hat{\phi}_0 = 1$ in the upper right corner, $\Omega^* > 0.95$ for L^* approaching 10^5, indicating that 95% of the possible extraction is achieved on a domain that is many orders of magnitude larger. The results are less impressive for $m = 1, 2$ because wider apertures provide less benefit when m is smaller. However, even in the most challenging case with $m = 1$ and $\hat{\phi}_0 = 100$, $\eta > 0.5$ for $L^* \leq 20$. Thus, even for this severe case, the introduction of transport channels permits a tenfold increase in medium size, from $L^* = 2$ to 20, without degrading the transport efficiency.

Results for several values of the capacitance parameter, $\hat{\phi}_0 \equiv \phi_0 \beta_0 / \beta_1$, are included in Fig. 5 for $m = 1$ and 2. For $m = 3$ results are shown only for $\hat{\phi}_0 = 1$. Since the nanopore porosity, ϕ_0, typically exceeds 0.1, and the nanopore capacitance, β_0, typically exceeds the transport channel capacitance, β_1, it is likely that $\hat{\phi}_0 > 0.1$. For this reason we emphasize larger values of $\hat{\phi}_0$. Note that the bending of the lines for $\hat{\phi}_0 = 0.1$ toward those for $\hat{\phi}_0 = 1.0$ indicates that the results for $\hat{\phi}_0 = 0.1$ are beginning to deviate from the asymptotic formulas that apply for small to moderate values of L^*. However, the approximate formulae still appear to provide reasonably good guidance for the expected range of application where $\hat{\phi}_0 > 0.1$ and $\eta > 0.5$. Before leaving Fig. 5, we note that all of the lines for $m = 1$ and 2 are terminated at the point where $a_1^* \approx 0.8 b_1^*$ and that this location roughly corresponds to an efficiency of $\eta \approx 0.4$.

To estimate the benefit gained by introduction of transport channels, suppose we desire a transport efficiency of at least $\Omega^* = 0.4$, for example. In the absence of transport channels this requires roughly that $\tanh L^*/L^* \geq 2.5$ and hence $L^* \leq 2.5$, consistent with the lowermost line in Fig. 5. In con-

trast, for the dual porosity system we can see from Fig. 5 that a value of $\Omega^* = 0.4$ corresponds to a condition where a_1^* $\sim 0.8 b_1^*$. At this intersection about half of the total volume is devoted to transport channels. From Eq. (22) it is further seen that this near equality of a_1^* and b_1^* implies that L^* $\sim (a_0^{*m} \hat{\phi}_0)^{-1/2}$. As a check on this approximation for parameter values of $a_0^* = 10^{-5}$ and $\hat{\phi}_0 = 1.0$, we can see that for $m = 1$ and $m = 2$, respectively, this simple formula yields reasonably accurate values of $L^* \sim 320$ and $L^* \sim 10^5$ as the locations where $\Omega^* \sim 0.4$ in Fig. 5. Keeping in mind the scaling of dimensionless variables, the above reasoning leads to the following estimates for the allowable increase in system size, L/L_r, for a given frequency or, alternatively, the allowable increase in frequency, ω/ω_r, for a given size:

$$\frac{L}{L_r} \sim \frac{1}{2}(a_0^{*m}\hat{\phi}_0)^{-1/2} \text{ and } \frac{\omega}{\omega_r} \sim \left[\frac{1}{2}(a_0^{*m}\hat{\phi}_0)^{-1/2}\right]^{4/(2+m)}. \tag{27}$$

Here, the subscript r refers to the reference configuration having no transport channels and $a_0^* \equiv a_0(\omega_r/4\alpha_0)^{1/2}$. Thus, the allowable size, L, and allowable frequency, ω, of the dual porosity system both increase strongly with increasing m and decreasing a_0^*.

Transitions from one transport regime to another may occur in systems having widely disparate pore sizes. In gas transport, for example, Knudsen diffusion may be operative in nanopores while, at the same time, viscous flow predominates in the larger transport pores. Similarly, different regimes may apply during different periods of time as, for example, a reduction in pressure increases the mean free path in a gas. In such circumstances, the benefits of transport channels are likely even greater than the estimates provided above. Optimization of these transitional systems can be based on results given here by using time-averaged properties and/or noninteger values of the exponent m, or by direct numerical integration of the governing equations.

B. Fixed diffusivity ratio between nanopores and transport channels ($m = 0$)

Before closing, we briefly address optimization of materials having transport diffusivities of nanopores and transport channels that are given by fixed constant values, α_0 and α_1, respectively. In contrast to all previous cases, α_1 no longer depends on the aperture a_1 of the transport channels. Hence, $m = 0$. This situation arises in ion transport applications where the nanopores are subject to hindered diffusion and/or surface-dominated capacitance while the transport pores are large enough to be relatively unaffected by these processes. Another application arises in conductive heat transfer where an energy storage material having high capacity but low conductivity is supplemented by a network of transport channels, or internal fins, containing a more conductive material.

This degenerate case for $m = 0$ is, in some ways, similar to the previous cases with $m > 0$. As before, there is an optimal value of a_1 for any given choice of b_1. But in this instance the optimum conditions are most conveniently expressed in terms of the optimal ratio of a_1 to b_1, as illustrated in Fig. 6.
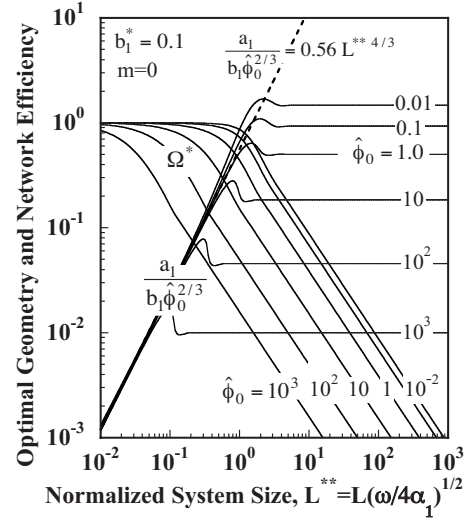

FIG. 6. Optimal geometric ratios and network efficiency, Ω^*, versus normalized system scale, L^{**}, for various choices of $\hat{\phi}_0$. Normalized results do not depend on the diffusivity ratio, α_1/α_0.

Here it is seen that for $b_1^* = 0.1$ the relationship among optimal variables is very well approximated by the following pair of expressions that respectively apply for small and large values of the system size:

$$\frac{a_1}{b_1\hat{\phi}_0^{2/3}} \approx 0.56 L^{**4/3} \text{ and } \frac{a_1}{b_1\hat{\phi}_0^{2/3}} \approx \text{constant.} \tag{28}$$

The lower asymptote is shown as a dotted line. The constant value that applies on the upper asymptote does depend on $\hat{\phi}_0$, but this dependence is shown for $\hat{\phi}_0$ ranging from 10^{-2} to 10^4. As apparent in Fig. 6, the constant on the right of Eq. (28) is close to unity for small values of $\hat{\phi}_0$ and it goes to $\hat{\phi}_0^{-2/3}$ (i.e., $a \approx b$) for large values of $\hat{\phi}_0$. Note that Eq. (28) and Figs. 6 and 7 employ a newly defined independent variable, L^{**}, which is scaled by α_1 instead of α_0,

$$L^{**} = L\left(\frac{\omega}{4\alpha_1}\right)^{1/2} = L^*\left(\frac{\alpha_0}{\alpha_1}\right)^{1/2}. \tag{29}$$

Use of this scaling eliminates any dependence of the normalized results on the prescribed diffusivity ratio, α_1/α_0. This can be seen by inspection of Eqs. (7)–(11) and was verified by numerical calculation.

In Fig. 7 it is seen that the above scaling of dependent and independent variables also collapses the results for values of b_1^* less than about 1.0. Since b_1^* is the Fourier number of the small scale, values much larger than unity indicate that the nanopores will not be well equilibrated, as indicated by the reduced values of Ω^* for $b_1^* = 2$. In analogy to the previous Fig. 6, we find that the asymptotes given in Eqs. (28) provide a fair approximation to the exact optima so long as $b_1^* \lesssim 1$. Agreement is excellent for $b_1^* \lesssim 0.1$.

In contrast to previous situations with $m > 0$, there is no longer an optimal choice of b_1^* for given values of L^{**} and $\hat{\phi}_0$. This is because there is no penalty for decreasing the aperture and spacing of the transport pores when $m = 0$. In
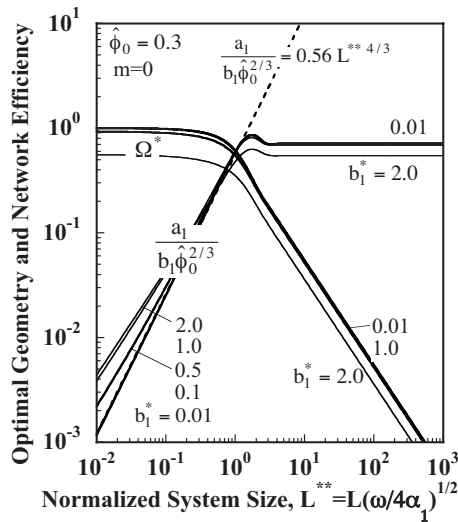
FIG. 7. Optimal geometric ratios and transport efficiency, Ω^*, versus normalized system scale, L^{**}, for various choices of normalized spacing, b_1^*.

this circumstance, it is always beneficial to decrease b_1^* thereby reducing the diffusion distance along the nanopores and improving uniformity over the small scale. As indicated by Eq. (28), the corresponding optimal value of aperture, a_1^* will necessarily shrink in proportion with b_1^*, but this does not reduce the diffusivity along the transport channels as it does when $m > 0$. Despite this general rule that smaller is better when $m = 0$, there is hardly any benefit gained by reducing the spacing to values less than $b_1^* \sim 1$, as apparent in Fig. 6.

IV. SUMMARY

Channel apertures and spacing have been optimized through analytical modeling of diffusionlike transport in a hierarchical network having transport channels that provide access to nanoscale pores. The model is applicable to viscous gas flow ($m = 2$) and Knudsen gas flow ($m \sim 1$) as well as simple diffusion ($m = 0$), and ion transport ($0 < m < 1$). These

exponents increase by unity when most of the capacitance is associated with channel surfaces.

Closed form expressions derived here can be used to compute channel dimensions that maximize transport to or from a porous storage medium for prescribed system scales and discharge times. The benefits gained by incorporation of transport channels are greatest when nanopores are very small and when the transport diffusivity depends strongly on pore size.

Physical interpretation of the system behavior is based on Fourier moduli representing ratios of diffusion time to desired discharge time. In optimized systems, the Fourier moduli for the nanopores and the transport channels are found to be of comparable magnitude indicating similar response times and similar drops in potential across the two scales. The ratio of the moduli depends mainly on the power-law exponent, m, with strict equality holding only for $m = 2$. Variations in optimal channel apertures and spacing with system size, response time, and other physical parameters have been explained, to a good approximation, by exploiting the observation that optimal Fourier moduli must remain of order unity for any choice of system parameters.

Optimal sizes and spacing of transport channels depend upon the desired time scale for extraction from a storage material. As a consequence, no multiscale storage material can be ideally suited for all applications. If slow extraction is acceptable, optimal transport channels will be narrower and sparser, leaving more of the system volume to accommodate nanopore storage or functionality. Conversely, systems optimized for rapid extraction will have wider more closely spaced transport channels.

[1] A. S. Arico, P. Bruce, B. Scrosati, J.-M. Tarascon, and W. Van Schalkwijk, Nature Mater. **4**, 366 (2005).

[2] *Adsorption and Transport at the Nanoscale*, edited by N. Quirke (CRC, Cleveland/Taylor & Francis, London, 2006).

[3] G. Q. Lu and X. S. Zhao, *Nanoporous Materials: Science and Engineering* (Imperial College Press, London, 2004).

[4] J. Chmiola, G. Yushin, Y. Gogotsi, C. Portet, P. Simon, and P. L. Taberna, Science **313**, 1760 (2006).

[5] G. Karniadakis, A. Beskok, and N. Aluru, *Microflows and Nanoflows: Fundamentals and Simulation* (Springer, New York, 2005).

[6] P. Dechadilok and W. M. Deen, Ind. Eng. Chem. Res. **45**, 6953 (2006).

[7] R. H. Nilson and S. K. Griffiths, J. Chem. Phys. **125**, 164510

(2006).

[8] G. B. West, J. H. Brown, and B. J. Enquist, Science **276**, 122 (1997).

[9] M. F. Laguna, S. Bohn, and E. A. Jagla, PLOS Comput. Biol. **4**, e1000055 (2008).

[10] J. R. Banavar, F. Colaiori, A. Flammini, A. Giacometti, A. Maritan, and A. Rinaldo, Phys. Rev. Lett. **78**, 4522 (1997).

[11] S. K. Khator and L. C. Leung, IEEE Trans. Power Syst. **12**, 1151 (1997).

[12] Y. Chen and P. Cheng, Int. J. Heat Mass Transfer **45**, 2643 (2002).

[13] S. Lorente and A. Bejan, J. Appl. Phys. **100**, 114909 (2006).

[14] F. Okkels and H. Bruus, Phys. Rev. E **75**, 016301 (2007).

[15] J. R. Banavar, A. Maritan, and A. Rinaldo, Nature (London)

399, 130 (1999).

[16] M. Durand, Phys. Rev. Lett. **98**, 088701 (2007).

[17] S. Bohn and M. O. Magnasco, Phys. Rev. Lett. **98**, 088702 (2007).

[18] A. Bejan and S. Lorente, J. Appl. Phys. **100**, 041301 (2006).

[19] J. W. Long, B. Dunn, D. R. Rolison, and H. S. White, Chem. Rev. **104**, 4463 (2004).

[20] C. Cercignani and A. Daneri, J. Appl. Phys. **34**, 3509 (1963).

[21] F. Sharipov, J. Micromech. Microeng. **9**, 394 (1999).

[22] O. G. Jepps, S. K. Bhatia, and D. J. Searles, Phys. Rev. Lett. **91**, 126102 (2003).

[23] M. W. Verbrugge and P. Liu, J. Electrochem. Soc. **152**, D79 (2005).

[24] H. Sakaguchi and R. Baba, Phys. Rev. E **76**, 011501 (2007).

[25] R. deLevie, Electrochim. Acta **8**, 751 (1963).

[26] G. E. Meyers, *Analytical Methods in Conduction Heat Transfer* (McGraw-Hill, New York, 1971).